TISSUE ENGINEERING: Part A
Volume 22, Numbers 1 and 2, 2016

DOI: 10.1089/ten.tea.2015.0087

termis
Tissue Engineering
& Regenerative Medicine
International Society

ORIGINAL ARTICLE

Tunable Microfibers Suppress Fibrotic Encapsulation via Inhibition of TGFβ Signaling

Jessica Allen, PhD,[*,1] Jubin Ryu, MD, PhD,[*,2] Alessandro Maggi, BS,[3] Bianca Flores,[1]
Julia R. Greer, PhD,[4] and Tejal Desai, PhD[1]

Fibrotic encapsulation limits the efficacy and lifetime of implantable biomedical devices. Microtopography has shown promise in the regulation of myofibroblast differentiation, a key driver of fibrotic encapsulation. However, existing studies have not systematically isolated the requisite geometric parameters for suppression of myofibroblast differentiation via microtopography, and there has not been *in vivo* validation of this technology to date. To address these issues, a novel lamination method was developed to afford more control over topography dimensions. Specifically, in this study we focus on fiber length and its effect on myofibroblast differentiation. Fibroblasts cultured on films with microfibers exceeding 16 μm in length lost the characteristic morphology associated with myofibroblast differentiation, while shorter microfibers of 6 μm length failed to produce this phenotype. This increase in length corresponded to a 50% decrease in fiber stiffness, which acts as a mechanical cue to influence myofibroblast differentiation. Longer microfiber films suppressed expression of myofibroblast-specific genes (α*SMA*, *Col1α2*, and *Col3α1*) and TGFβ signaling components (*TGFβ1*, *TβR2*, and *Smad3*). About 16 μm long microfiber films subcutaneously implanted in a mouse wound-healing model generated a substantially thinner fibrotic capsule and less deposition of collagen in the wound bed. Together, these results identify a critical feature length threshold for microscale topography-mediated repression of fibrotic encapsulation. This study also demonstrates a simple and powerful strategy to improve surface biocompatibility and reduce fibrotic encapsulation around implanted materials.

Introduction

Chronic foreign body responses and resultant fibrotic encapsulation pose one of the primary obstacles facing implantable sensors or therapeutic delivery devices. This complication limits the lifetime of the device by impairing the flow of nutrients and analytes, and delivery of therapeutics into the host tissue.[1–3]

Fibrotic encapsulation is initiated by fibroblast recruitment to the site of implantation. Recruited fibroblasts subsequently differentiate into myofibroblasts in response to the growth factor TGFβ, and to mechanical tension present in the wound space.[4,5] TGFβ activates expression of alpha smooth muscle actin (αSMA) and collagen, the major protein component of the fibrotic capsule.[5] The intracellular mechanisms involved in promotion of the myofibroblast phenotype via mechanosensing are still largely unknown, but they correlate with increased actin stress fiber formation, generation of internal cellular tension, and elongated cell shape.[4]

Mechanical cues have been found to regulate the TGFβ pathway in a variety of contexts, and therefore it is likely that these two types of cues closely interact to regulate myofibroblast differentiation and fibrotic encapsulation.[6–8] In fact, it is well known that compliant materials can reduce the activation of the TGFβ pathway and myofibroblast differentiation.[4,7–11] However, a method to leverage this knowledge into effective product design remains elusive.

Multiple strategies have been proposed to circumvent fibrotic encapsulation, primarily focusing on material biocompatibility and co-delivery of anti-inflammatory agents, which limit and add complexity to device design, respectively.[2,3,12] In addition, previous studies have demonstrated that topography—a cue that can directly affect cell

[1]UCSF Department of Bioengineering and Therapeutic Sciences, San Francisco, California.
[2]UCSF Department of Dermatology, San Francisco, California.
[3]California Institute of Technology, Department of Medical Engineering, Pasadena, California.
[4]California Institute of Technology, Division of Engineering and Applied Science, Kavli Nanoscience Institute, Pasadena, California.
*Co-first authors.

differentiation and behavior in a variety of contexts—may also be utilized to reduce the fibrotic response.[11,13–26] One advantage of topography, especially at the micro and nanoscale, is that it could conceivably alter the surface mechanics as perceived by cellular interaction without greatly altering the design of implanted devices on the macroscale.[27]

Of particular interest to implanted devices, Kam *et al.* demonstrated that high-aspect ratio microfibers, produced by imprint lithography, reduced fibroblast proliferation and differentiation *in vitro*.[19] These high-aspect ratio microfibers may represent a method to leverage the well-documented effect of compliant materials on fibroblast behavior into a material that can be applied therapeutically or as an improvement to current designs. However, this study compared a variety of geometries without a systematic isolation of specific topographical feature dimensions (e.g., fiber height or width), making it difficult to identify the minimum necessary physical parameters that lead to knockdown of the fibrotic response via topography. Moreover, it is unknown whether this effect would be replicated *in vivo.*

In this article, we describe a novel lamination method to create microscale fibers. This approach yields microfibers that match topography previously shown to reduce myofibroblast differentiation, and allows fiber length to be tuned by varying the lamination rate. Fibroblasts grown on long microfiber films reduce expression of myofibroblast markers, and components of the TGFβ pathway. Murine implantation studies demonstrate the antifibrotic potential of these microfiber films *in vivo*, with a dramatic reduction in collagen deposition around the implanted films, and alteration of the fibroblastic morphology surrounding the film. These studies validate a simple way to reduce myofibroblast differentiation and prevent fibrotic encapsulation *in vivo,* thereby improving the performance and longevity of implanted biomedical devices.

Results

Microfiber geometry and stiffness are defined by a simple lamination method

To determine the effect of fiber length on fibroblast morphology, polypropylene films with 1 μm diameter microfibers of either 6 μm (''short'') or 16 μm (''long'') lengths were fabricated using a simple lamination method (Fig. 1). Briefly, microfiber height was controlled by polypropylene lamination speed while diameter was controlled by the pore size of the negative polycarbonate template. To determine the change in surface energy with the addition of microfibers, half angle measurements were completed on each type of film. While the half angle did change with the addition of microfibers on polypropylene films, the angle is not significantly different between short and long microfiber films, suggesting addition of microfibers results in a similar shift in surface energy for the polypropylene film (Supplementary Fig. S1; Supplementary Data are available online at www.liebertpub.com/tea).

Nanoindentation was used to identify the relative stiffness of the fibers under compressive load. Using a flat punch diamond nanoindenter tip with a 10 μm square cross section, the microfibers were compressed in the G200 nanoindenter at a constant prescribed displacement rate of 10 nm/s. Figure 2a, b show representative load versus displacement data for short and long microfiber films, respectively. The linear portion of the unloading curve was used to estimate the microfiber stiffness. It is important to note that the stiffness experienced by a cell on a microfiber film depends on the deflection of the microfibers in contact with the cell. Therefore, relative stiffness was reported. Our experiments revealed that the long microfibers were less than half as stiff as short microfibers, offering a less rigid interface for attached cells (Fig. 2c).

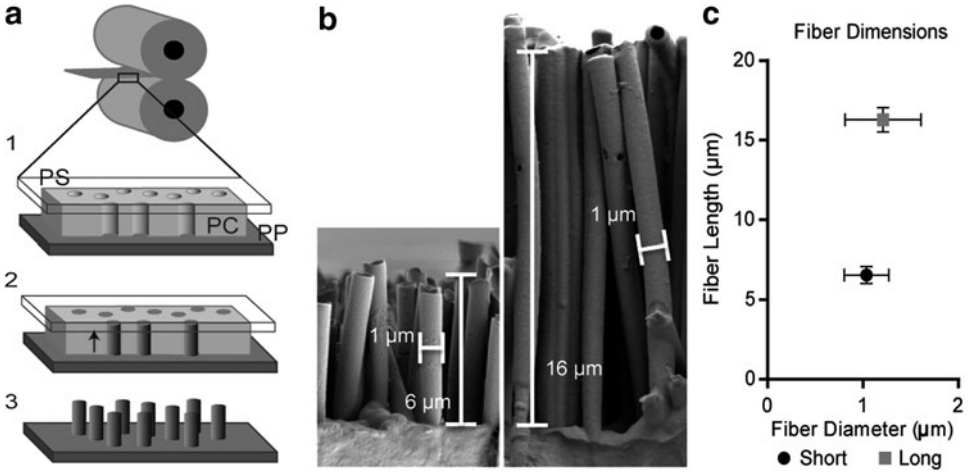

FIG. 1. Lamination creates microfibers with defined and tunable geometries. **(a)** (1) A microporous polycarbonate membrane (PC) is placed between a thin layer of polystyrene (PS) and a polypropylene film (PP). (2) The layers are pressed between two rollers at 200°C and 20 psi, melting the PP into the microporous membrane. (3) Methylene chloride is used to etch away the PC, leaving a microstructured film. **(b)** Scanning electron microscopy (SEM) images demonstrate microfiber geometry. **(c)** Measurements of imaged microfibers reveal uniform fiber diameter and fiber length within long and short fiber films ($n \geq 5$).

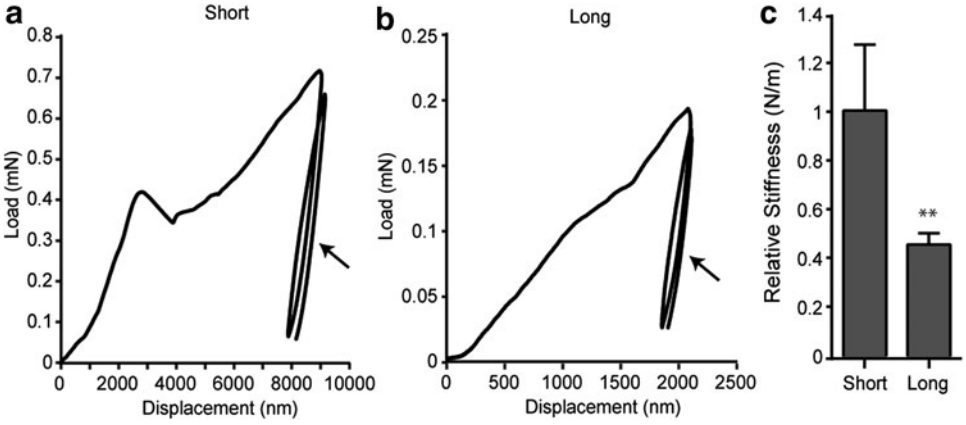

FIG. 2. Relative stiffness decreases as microfiber length increases. Representative load deformation curves for the compression of short **(a)** and long **(b)** microfibers. Microfiber stiffness was determined from the slope of the unloading curve (*arrow*). **(c)** The relative stiffness of short microfibers is twice that of the long microfibers (**$p < 0.01$, $n \geq 12$).

Characteristic myofibroblast morphology and gene expression are suppressed on long microfiber films

Murine 3T3 fibroblasts cultured on both short and long microfiber films were imaged by scanning electron microscopy (SEM) and compared to fibroblasts cultured on flat polypropylene film controls. SEM images reveal a progressive change in fibroblast morphology as fiber length increases (Fig. 3a). On flat controls and short microfiber films, fibroblasts possess elongated projections that emanate

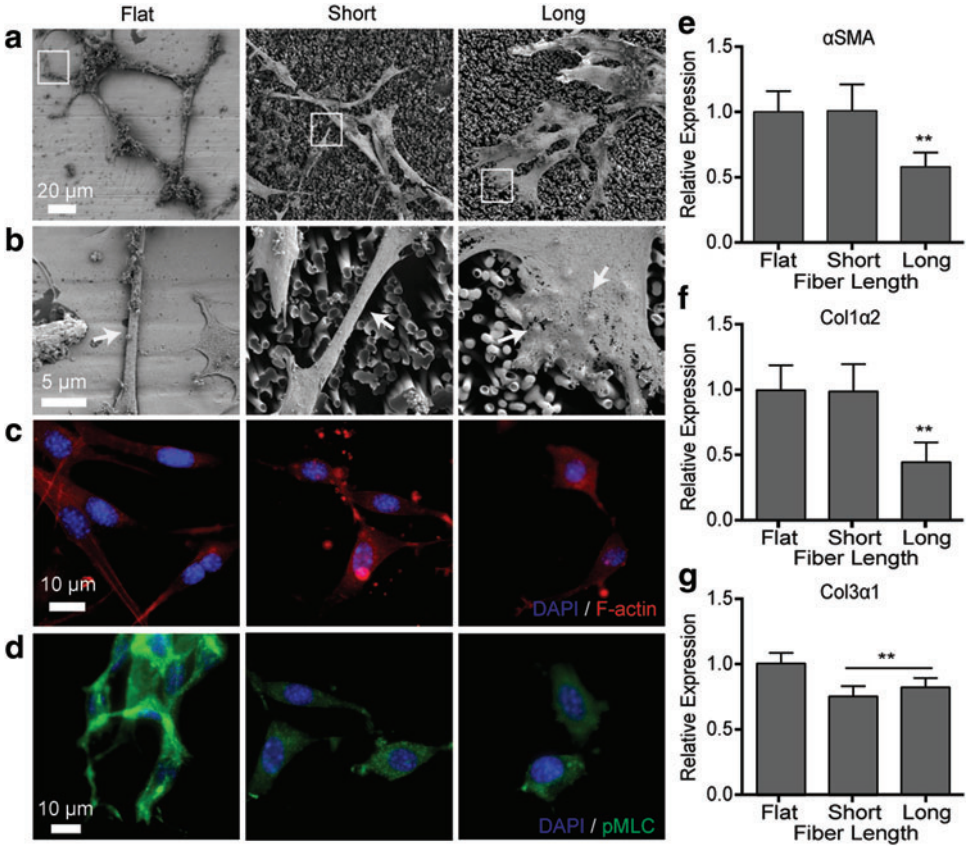

FIG. 3. Characteristic myofibroblast phenotype is selectively suppressed by long microfiber films. **(a)** SEM images reveal that 3T3 fibroblasts on long (16 μm) microfibers lose the characteristic morphology and tense, linear projections classically associated with myofibroblast differentiation ($n = 3$). *White boxes* indicate areas of high magnification shown in Fig. 3b. **(b)** High magnification images of cellular projections reveal differences in cytoskeletal network density and arrangement on flat, short fiber, and long fiber films (*white arrows*). The linearity and density of the cytoskeleton decreases with increasing fiber length, with the cells loosely draped over the fibers on long microfiber films. **(c)** Rhodamine phalloidin staining of filamentous actin (F-actin) (*red*) reveals a loss of stress fiber formation in 3T3 fibroblasts cultured on short and long microfiber films ($n \geq 5$). **(d)** Staining for phosphorylation of myosin light chain (pMLC) (*green*) is dramatically reduced in 3T3 fibroblasts cultured on short and long microfibers compared with flat film controls ($n \geq 5$). **(e–g)** As microfiber length increases, expression of myofibroblast-specific genes alpha smooth muscle actin (α*SMA*) and *Col1*α*2* progressively decreases at 48 h. *Col3*α*1* expression is modestly reduced on both long and short fibers (**$p < 0.01$, $n \geq 5$). Color images available online at www.liebertpub.com/tea

from the central cell body and appear rigid. In contrast, on long microfiber films, fibroblasts are devoid of these linear projections and instead adopt a more trapezoidal, less spindled morphology. High magnification SEM images of the cellular projections reveal additional differences between flat, short, and long microfiber films (Fig. 3b). On flat and short microfiber films, the cellular projections are comprised of dense, linear cytoskeletal networks. On long microfiber films, the cytoskeletal network is less prominent and loosely draped over the topography, in contrast to the dense, linear network in fibroblasts grown on short microfiber and flat films.

To determine whether the differences in morphology seen in the SEM images correlate with changes in the actin cytoskeleton, cells were stained for filamentous actin (F-actin) using rhodamine phalloidin (Fig. 3c). Fibroblasts cultured on flat films form prominent stress fibers with multiple vertices along the cell perimeter, reflecting points of attachment to the substrate. In contrast, fibroblasts grown on either the short or long microfiber films have less prominent stress fibers and a more rounded cell shape with fewer vertices.

Changes in cell morphology and stress fiber formation suggest that exposure to microfiber films may alter intracellular tension generation. Phosphorylation of myosin light chain (pMLC) induces intracellular tension along actin stress fibers, and 3T3 fibroblasts were therefore stained for pMLC after 48 h of culture (Fig. 3d). Compared with cells grown on flat films, pMLC staining in fibroblasts cultured on short or long microfibers adopts a more diffuse pattern, indicating a decrease in myosin contractile activity and internal cellular tension. Staining intensity on long and short fibers was significantly decreased compared with that on flat films (Supplementary Fig S2).

The morphological and cytoskeletal changes in fibroblasts noted above suggest myofibroblast differentiation is selectively decreased on long microfibers, most likely in response to an increase in compliance at the interface. To determine the effect of microfiber length on myofibroblast differentiation, 3T3 fibroblasts were cultured on microfiber films for 48 h in the presence of TGFβ1 to induce differentiation toward the myofibroblast phenotype. While culture on short microfiber films had no statistically significant effect compared to flat controls, culture on long fibers reduced expression of *αSMA* and *Col1α2* by 40% and 60%, respectively (Fig. 3e, f). Expression of *Col3α1* was more modestly reduced on both long and short microfiber films, reaching 20% at 48 h (Fig. 3g). Therefore, microfibers beyond a critical length appear to selectively reduce myofibroblast-specific gene expression.

Long microfibers suppress activation of the TGFβ pathway

As TGFβ directly regulates myofibroblast gene expression, the effect of microfiber length on this signaling pathway was analyzed. Fibroblasts cultured for 48 h on both short and long microfiber films exhibited a reduction in gene expression of TGFβ signaling components, including TGFβ1 ligand (*TGFβ1*), TGFβ1 receptor 2 (*TβR2*), and the transcription factor *Smad3* (Fig. 4a). However, consistent with the expression patterns of αSMA and Col1α2, knockdown of TGFβ signaling was most pronounced in fibroblasts cultured on long microfiber films, with a 50% or greater reduction in all TGFβ signaling genes compared with flat controls.

As *Smad3* RNA expression was reduced by culture on microfiber films, Smad nuclear localization, which indicates activation of Smad by TGFβ, was assessed in 3T3 fibroblasts by immunofluorescence. After 48 h, Smad 2/3 staining intensity is markedly decreased in short and long microfibers (Fig. 4b). Compared with bright nuclear staining on flat films, fibroblasts on short microfiber films have a significant reduction in nuclear staining intensity, with small regions of focal hyperintensity that localize to the nucleoli. On long microfiber films, nuclear Smad2/3 is even further decreased and diffusely distributed, with no regions of localized intensity. Smad3 (and to a lesser extent Smad2) acts as a transcription factor to upregulate *αSMA, Col1α2,* and *Col3α1* gene expression.[28–33] Therefore, the suppression of myofibroblast specific genes in fibroblasts cultured on long microfiber films may result from this reduction of Smad2/3 activation and nuclear localization, reducing its availability for transcriptional regulation.

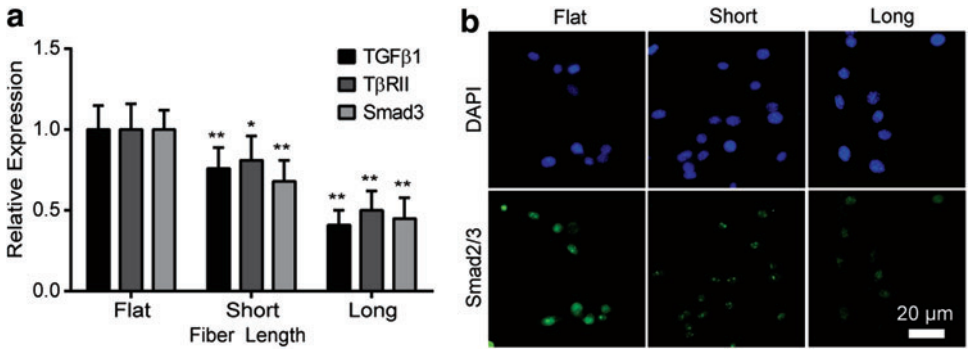

FIG. 4. TGFβ pathway signaling progressively decreases with increasing microfiber length. **(a)** As microfiber length increases, *TGFβ1*, *TβR2*, and *Smad3* expression is reduced. Knockdown of TGFβ signaling is most pronounced on long microfiber films. **(b)** Similar to trends in TGFβ gene expression, Smad2/3 nuclear localization (in *green*) is progressively reduced as microfibers increase in length. Nuclei are marked by DAPI stain in *blue* ($*p<0.05$, $**p<0.01$, $n\geq3$). Color images available online at www.liebertpub.com/tea

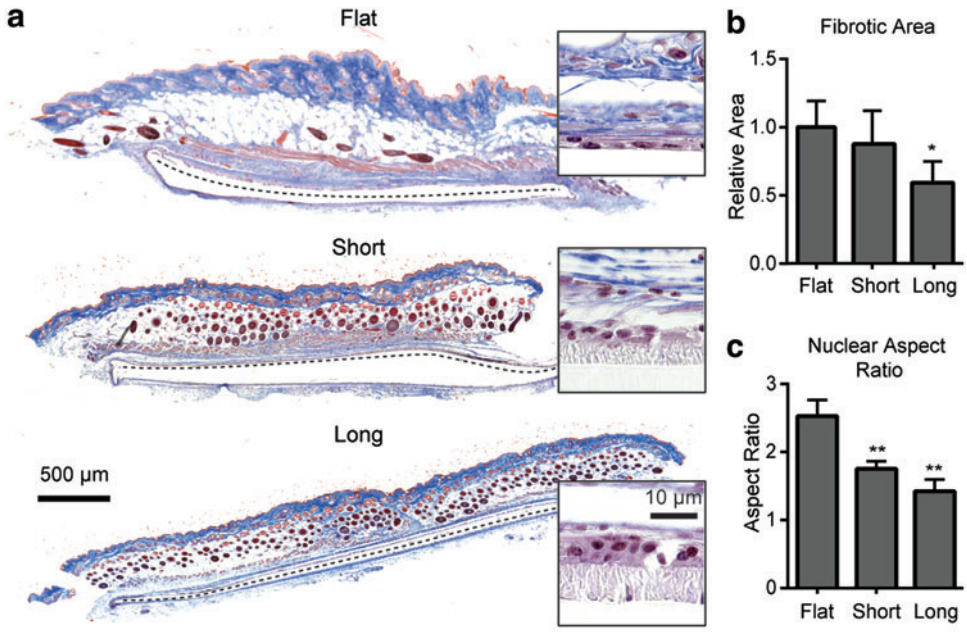

FIG. 5. Fibrotic encapsulation is reduced around long microfiber films *in vivo*. **(a)** Trichrome-stained histological sections demonstrate a decrease in collagen-rich regions (*blue*) around first short and then long microfiber films compared with flat controls (*black dashed line* marks film location). Higher magnification images reveal that fibroblast nuclei adjacent to the film interface become progressively rounder on first short and then long microfiber films, in contrast to classic spindle-shaped fibroblasts found at the flat film interface (*inset* photos). **(b)** Quantification of fibrotic area reveals a 41% decrease in collagen deposition around the microfiber films relative to flat controls. **(c)** Quantification of nuclear aspect ratio demonstrates that nuclei in proximity to long microfiber films are more rounded compared to nuclei near flat controls, which are more elongated and spindled. Nuclei in proximity to short microfiber films have an intermediate aspect ratio ($*p < 0.05$, $**p < 0.01$, $n \geq 5$). Color images available online at www.liebertpub.com/tea

Long microfiber films inhibit fibrotic encapsulation in vivo

The above *in vitro* experiments suggest that long microfiber films reduce myofibroblast differentiation, and therefore could reduce scar tissue production and encapsulation *in vivo*. To determine the performance of microfiber films *in vivo*, flat, short, and long microfiber films were subcutaneously implanted in wild-type adult mice. At 2 weeks postsurgery, histologic analysis with Masson's trichrome stain shows sparser deposition of collagen (in blue), and a 41% reduction in the fibrotic area in wounds treated with long microfiber films (Fig. 5a, b). Short microfiber films did not significantly reduce collagen deposition compared with flat controls.

Additionally, at high-power magnification, a change in fibroblast morphology within the wound bed is also observed (Fig. 5a, inset photos). In wound beds treated with flat films, fibroblast nuclei adopt an elongated, spindled morphology that is classically associated with myofibroblast differentiation. In contrast, fibroblasts observed at the interface of the long microfiber films have nuclei that are much more rounded with an aspect ratio closer to 1. Nuclei at the interface of short microfiber films have an intermediate aspect ratio between that of the flat and long microfiber films (Fig. 5c). These differences in morphology mirrors the changes in 3T3 fibroblast morphology seen *in vitro* via SEM and immunofluorescence.

To further assess collagen deposition around flat or microfiber films *in vivo*, immunofluorescence staining was performed (Fig. 6a). Deposition of collagen I is selectively reduced by 39% at the interface of the long microfiber films, while there is no significant change in collagen III staining (Fig. 6b, Supplementary Fig S3).

In wound beds treated with flat and short microfiber films, high magnification images demonstrate that immunofluorescence is most intense directly above and below the pocket containing the inserted film (Fig. 6c). In contrast, wound beds treated with long microfiber films have differential staining, such that intense staining for collagen I is found inferior to the film, while staining is nearly absent superior to the long microfiber film. This differential intensity is noteworthy because microfibers are only present on the superior side of the inserted film. The inferior side of the microfiber film is flat and therefore acts as an internal control, inducing a similar collagen staining intensity to that found at both interfaces of the flat film.

Discussion

We demonstrate that a specific microtopography may be used to decrease fibrotic encapsulation *in vivo* by diminishing myofibroblast differentiation via suppression of TGFβ signaling. Our versatile lamination method for microfiber fabrication allows controllable variations in geometry by simply adjusting lamination speed or polycarbonate membrane pore size and spacing. Controlling the geometry of the presented topography allowed isolation of microfiber length for study as a regulator of myofibroblast differentiation.

While the topography itself can impact fibroblast differentiation (by altering the conformation, concentration of the adsorbed proteins, and available attachment area that may in

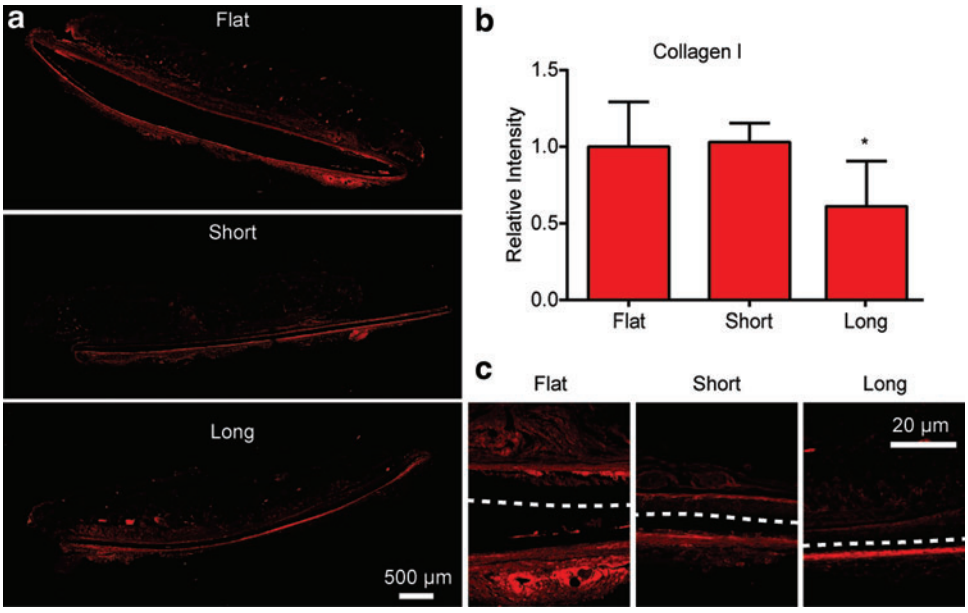

FIG. 6. Collagen deposition is reduced around long microfiber films *in vivo*. **(a)** Immunofluorescent staining for collagen reveals a reduction in collagen I deposition around long microfiber films compared with short microfiber films and flat controls. **(b)** Deposition of collagen I, as quantified by staining intensity, is significantly decreased above long microfiber films. **(c)** Higher magnification images demonstrate that collagen deposition is not uniform around long microfiber films, as it is around short microfiber films and flat film controls (*white dashed line*). Collagen I staining is absent in the tissue exposed to the superior, long microfiber-presenting side of the film, contrasting with intense staining in the tissue exposed to the flat inferior side of the film ($*p < 0.05$, $n \geq 5$). Color images available online at www.liebertpub.com/tea

turn effect integrin engagement, filopodia formation, and myofibroblast differentiation), dramatic repression of differentiation is only observed on long microfibers, compared to relatively mild effects on short microfibers.[13,17,19,34–36] Long microfibers are most likely interpreted by the cell as an increase in compliance, as increased microfiber length presents a more deformable interface. Therefore, the reduction in myofibroblast differentiation is likely in response to mechanosensing of a compliant material.[4,7,9,17,37] It is also likely that suppression of TGFβ signaling is in response to perceived compliance, as interaction between the TGFβ pathway and mechanosensing has been identified in numerous contexts, including mechanisms that appear to directly affect Smad activation and localization, similar to the observations described in this study.[6–8]

While wound beds treated with microfibers demonstrated a dramatic reduction in collagen deposition and fibrotic response at 2 weeks, it should be noted that a minor fibrotic response still developed around the microfiber film. Moreover, only one time point was investigated. A time course of a month or more would be necessary to determine the full effect of the microfiber films on fibrotic encapsulation. Nevertheless, the reduction in the thickness and density of the capsule surrounding the microfiber film suggests that microfibers could improve diffusion of therapeutics and analytes to and from implantable devices and may represent a viable strategy in reduction of postoperative scarring.

Microfibers induce changes in nuclear morphology *in vivo* that mirror changes seen *in vitro* suggesting similar mechanisms are involved in both contexts.[15] Future work should assess the effect of microfibers on other aspects of the inflammatory response, including recruitment of macrophages and other inflammatory cells. Moreover, although previous work indicates that a similar effect can be seen on polystyrene microtopography[19], polymers other than polypropylene should be investigated to determine the optimal material for the reduction of the fibrotic response using microfibers.

Conclusions

We report a novel synthesis strategy to reproducibly create microscale topography. Using this approach, we define specific geometric parameters that suppress myofibroblast differentiation via inhibition of the TGFβ pathway. Additionally, we demonstrate that these microfibers can reduce fibrotic encapsulation *in vivo*, highlighting their potential to prevent encapsulation of implantable biomedical devices.

Experimental Section

Microfiber film fabrication

Microfiber films were fabricated by laminating polypropylene films into microporous polycarbonate membranes in a hot roll laminator (Cheminstruments, HL-100), as described previously (Fig. 1a).[38] Briefly, polystyrene (182427; Sigma), dissolved in toluene (10% w/v), was spin-cast on to a polyethylene terephthalate (PET) backing layer. The polystyrene was used to cap a microporous polycarbonate membrane (ATTP04700; Millipore), which was then overlaid on prepressed polypropylene film (TF-225–4; Lab Supply). All layers were pressed through the hot roll

laminator at 20 psi and 210°C. Lamination speed was used to control fiber length, with short fibers pressed at 0.7 mm/s and long fibers at 0.2 mm/s (Fig. 1b). Polycarbonate and polystyrene was then etched away in two serial washes in methylene chloride for 8 min each. All experiments were compared to flat polypropylene film controls processed as above but without the overlaid microporous membrane. Microfiber length and diameter were measured in ImageJ from SEM images and averaged from a minimum five film samples. Figure 1c shows the mean and standard deviation of the fiber dimensions for representative ''long'' and ''short'' microfiber films. ANOVA analysis followed by Student–Newman–Keuls test was used to evaluate statistical significance.

Half angle measurements

The surface energy of flat and microfiber films was assessed with half angle measurements using a CAM-Plus Micro/Film Contact Angle Meter (Cheminstrucments). The half angle was measured for a droplet of $\sim$20 μL of water. Three films per topography were tested, with droplets applied to three separate locations for each film. ANOVA analysis followed by Student–Newman–Keuls test was used to evaluate statistical significance.

Nanoindentation

Microfiber films were compressed in air using the XP module of Agilent's nanoindenter G200 with a custom-made diamond flat punch indenter tip with a 10 μm square cross section. Compressions were performed at a constant prescribed displacement rate of 10 nm/s through a feedback loop. Approximately 12 fibers were simultaneously compressed under the flat punch to depths ranging from 30% to 90% of the lengths of the straight fibers. Two load-unload cycles were performed for each sample with a hold segment of 1 s at peak displacement. At least five tests were performed for each compression depth. ANOVA analysis followed by Student–Newman–Keuls test was used to evaluate statistical significance. Calculated stiffnesses were compared to the harmonic contact stiffness acquired during the experiment at the data acquisition rate of $\sim$150 Hz to ensure full contact (Supplementary Fig S4).

Cell culture

Murine 3T3 fibroblasts were used for all *in vitro* studies. Growth media for 3T3 fibroblasts consisted of Dulbecco's modified Eagle's medium high glucose with 10% fetal bovine serum, 1% sodium pyruvate, and 1% penicillin/streptomycin. Experiments were performed in differentiation media consisting of growth media supplemented with 5 ng/mL TGFβ1 (100–21; Peprotech).

SEM imaging

To prepare cells adhered to microfiber films for SEM imaging, cells were fixed in 4% paraformaldehyde in phosphate buffered saline (PBS) for 15 min at room temperature. Drying was performed in 100% ethanol with a critical point dryer (Tousimis). Samples of microfiber films with and without cells were coated with 10 nm of iridium before imaging in a Carl Zeiss Ultra 55 Field Emission Scanning Electron Microscope using an in-lens SE detector at a beam voltage of 2 kV and a working distance of $\sim$6 mm.

Immunofluorescence

After 48 h of culture, cells were fixed in 4% paraformaldehyde in PBS for 15 min at room temperature, permeabilized in PBS with 0.5% Triton X-100 for 5 min, and blocked for 1 h in 10% goat serum. Primary antibodies were diluted in PBS with 2% goat serum and 3% Triton X-100 and incubated overnight at 4°C at the following concentrations: Smad2/3 antibody 1:400 (sc8332; Santa Cruz); pMLC 1:50 (#3671; Cell Signaling). Secondary goat anti-rabbit Alexa Fluor 488 (A11034; Invitrogen) was added at a dilution of 1:400 for 1 h at room temperature. For F-actin staining, rhodamine phalloidin (R415; Invitrogen) was diluted to 1:800 in PBS and incubated with fixed cells for 20 min at room temperature. Nuclei were counterstained in Hoechst dye and cells were visualized using a Nikon Ti-E Microscope. Images were processed in Image J and normalized to species-matched IgG controls. All figures are representative images for three or more biological replicates.

Quantitative polymerase chain reaction

RNA was isolated using RNeasy column purification (74104; Qiagen). The concentration and purity of RNA was determined using a Nanodrop ND-1000 Spectrophotometer (Thermo Scientific). Approximately 1 μg of RNA was converted to cDNA in a reverse transcription reaction using the iScript cDNA Synthesis Kit (170–8891; Bio-Rad). Quantitative polymerase chain reaction (PCR) analysis of each sample was performed in a ViiA 7 Real-Time PCR System (Life Technologies). Forward and reverse intron-spanning primers (Supplementary Table S1) and Fast SYBR Green Master Mix (4385612; Life Technologies) were used to amplify each cDNA of interest. Each sample was run in duplicate and all results were normalized to the housekeeping gene *L19*. Fold changes in gene expression were calculated using the delta-delta Ct method.[39] Figures show the mean and standard deviation for a minimum of five biological replicates. For statistical analysis, average expression and standard error of the mean were calculated for each condition across all biological replicates, each of which is an average of two technical replicates. ANOVA analysis followed by Student–Newman–Keuls test was used to evaluate statistical significance.

In vivo *studies and histology*

Six-week-old female Swiss-Hamster mice were used for our *in vivo* studies. Mice were anesthetized with intraperitoneal Avertin. On the dorsal aspect of each mouse, two 0.6 cm incisions were made and a subcutaneous pocket was dissected using surgical microscissors. In the contralateral wounds, each mouse was implanted with either a flat control or a microfiber film, and the surgical wounds were closed with nonabsorbable sutures. Two weeks after device placement, the mice were anesthetized, and both dorsal surgical sites were excised using a 0.8 cm punch biopsy. Tissue samples were fixed for 24 h in 4% paraformaldehyde and paraffin embedded. Sections were then either stained with Masson's Trichrome stain, or deparaffinized and immunostained for collagen I and III. For immunostaining, the samples were blocked in 4% bovine serum albumin, and the

following antibodies were used: mouse anti-collagen I at 1:100 dilution (80565; Santa Cruz), goat anti-collagen III at 1:100 dilution (8781; Santa Cruz), anti-mouse Alexa 568 at 1:500 dilution (Invitrogen), and anti-goat Alexa 488 at 1:500 dilution (Invitrogen). Fibrotic area was calculated from 19 images (7 flat controls, 5 short, and 7 long microfiber films) by drawing a region of interest around the fibrotic capsule, highlighted in blue by Masson's Trichrome stain. Nuclear aspect ratio was calculated from 19 images (7 flat controls, 5 short, and 7 long microfiber films) by measuring the long and short axis of cellular nuclei (highlighted by in purple by Trichrome stain) and dividing length by width for each measured nuclei. Collagen I and III intensity was calculated from 19 images (7 flat controls, 5 short, and 7 long microfiber films) by dividing the absolute intensity of immunofluorescence by the area of the fibrotic capsule. All measurements were performed in a blinded fashion. Immunostained images were obtained using Nikon Elements software and normalized to species-matched IgG controls. ANOVA analysis followed by Student–Newman–Keuls test was used to evaluate statistical significance.

Acknowledgments

The authors would like to thank R. Fearing and A. Gillies at the Berkeley Biomimetic Millisystems Lab for sharing their expertise in microscale topography and granting us access to their lamination equipment. We gratefully acknowledge use of the Carl Zeiss Ultra 55 FE-SEM and supporting equipment at SF State. The FE-SEM and supporting facilities were obtained under NSF-MRI award #0821619 and NSF-EAR award #0949176, respectively. We would also like to acknowledge B. Hann and D. Wang for their aid in development and execution of the *in vivo* studies. This work was funded by the National Science Foundataion (NSEC). J. R. Greer and A. Maggi gratefully acknowledge the financial support of Caltech's EAS Discovery Funds.

Disclosure Statement

No competing financial interests exist.

References

1. Jung, K.I., Lee, S.-B., Kim, J.H., and Park, C.K. Foreign body reaction in glaucoma drainage implant surgery. Invest Ophthalmol Vis Sci **54,** 3957, 2013.
2. Dang, T.T., *et al.* Enhanced function of immuno-isolated islets in diabetes therapy by co-encapsulation with an anti-inflammatory drug. Biomaterials **34,** 5792, 2013.
3. Santos, E., Pedraz, J.L., Hernández, R.M., and Orive, G. Therapeutic cell encapsulation: ten steps towards clinical translation. J Control Release **170,** 1, 2013.
4. Tomasek, J.J., Gabbiani, G., Hinz, B., Chaponnier, C., and Brown, R.A. Myofibroblasts and mechano-regulation of connective tissue remodelling. Nat Rev Mol Cell Biol **3,** 349, 2002.
5. Li, A.G., *et al.* Elevation of transforming growth factor beta (TGF b) and its downstream mediators in subcutaneous foreign body capsule tissue. J Biomed Mater Res A **82,** 498, 2007.
6. Allen, J.L., Cooke, M.E., and Alliston, T. ECM stiffness primes the TGFbeta pathway to promote chondrocyte differentiation. Mol Biol Cell **23,** 3731, 2012.
7. Huang, X., *et al.* Matrix stiffness-induced myofibroblast differentiation is mediated by intrinsic mechanotransduction. Am J Respir Cell Mol Biol **47,** 340, 2012.
8. Wipff, P.-J., Rifkin, D.B., Meister, J.-J., and Hinz, B. Myofibroblast contraction activates latent TGF-beta1 from the extracellular matrix. J. Cell Biol **179,** 1311, 2007.
9. Hinz, B. The myofibroblast: paradigm for a mechanically active cell. J Biomech **43,** 146, 2010.
10. Hinz, B. Tissue stiffness, latent TGF-beta1 activation, and mechanical signal transduction: implications for the pathogenesis and treatment of fibrosis. Curr Rheumatol Rep **11,** 120, 2009.
11. Mateos-Timoneda, M.A., Castano, O., Planell, J.A., and Engel, E. Effect of structure, topography and chemistry on fibroblast adhesion and morphology. J Mater Sci Mater Med **25,** 1781, 2014.
12. Orive, G., Tam, S.K., Pedraz, J.L., and Hallé, J.-P. Biocompatibility of alginate-poly-L-lysine microcapsules for cell therapy. Biomaterials **27,** 3691, 2006.
13. Ayala, P., and Desai, T.A. Integrin α3 blockade enhances microtopographical down-regulation of α-smooth muscle actin: role of microtopography in ECM regulation. Integr Biol (Camb). **3,** 733, 2011.
14. Ayala, P., Lopez, J.I., PhD, and Desai, T.A. Microtopographical cues in 3D attenuate fibrotic phenotype and extracellular matrix deposition : implications for tissue regeneration. Tissue Eng Part A **16,** 2519, 2010.
15. Bettinger, C.J., Langer, R., and Borenstein, J.T. Engineering substrate topography at the micro- and nanoscale to control cell function. Angew Chem Int Ed Engl **48,** 5406, 2009.
16. Clark, P., Connolly, P., Curtis, A.S., Dow, J.A, and Wilkinson, C.D. Cell guidance by ultrafine topography in vitro. J Cell Sci **99,** 73, 1991.
17. Dalby, M.J., Riehle, M.O., Johnstone, H., Affrossman, S., and Curtis, A.S. Investigating the limits of filopodial sensing: a brief report using SEM to image the interaction between 10 nm high nano-topography and fibroblast filopodia. Cell Biol Int **28,** 229, 2004.
18. Kam, K.R., *et al.* Nanostructure-mediated transport of biologics across epithelial tissue: enhancing permeability via nanotopography. Nano Lett **13,** 164, 2013.
19. Kam, K.R., *et al.* The effect of nanotopography on modulating protein adsorption and the fibrotic response. Tissue Eng Part A **20,** 130, 2014.
20. Lam, M.T., Clem, W.C., and Takayama, S. Reversible on-demand cell alignment using reconfigurable microtopography. Biomaterials **29,** 1705, 2008.
21. McGarry, J.P., *et al.* Simulation of the contractile response of cells on an array of micro-posts. Phil Trans A Math Phys Eng Sci **367,** 3477, 2009.
22. McNamara, L.E., *et al.* Nanotopographical control of stem cell differentiation. J Tissue Eng **18,** 120623, 2010.
23. Muthusubramaniam, L., Zaitseva, T., Paukshto, M., Martin, G., and Desai, T. Effect of collagen nanotopography on keloid fibroblast proliferation and matrix synthesis : implications for dermal wound healing. Tissue Eng Part A **20**, 2728, 2014.
24. Bettinger, C.J., Kulig, K.M., Vacanti, J.P., Langer, R., and Borenstein, J.T. Nanofabricated collagen-inspired synthetic elastomers for primary rat hepatocyte culture. Tissue Eng Part A **15,** 1321, 2010.
25. Pot, S.A., *et al.* Nanoscale topography–induced modulation of fundamental cell behaviors of rabbit corneal keratocytes, fibroblasts, and myofibroblasts. Invest Ophthalmol Vis Sci **51,** 1373, 2010.

26. Dalby, M., *et al.* Fibroblast reaction to island topography: changes in cytoskeleton and morphology with time. Biomaterials **24,** 927, 2003.
27. Harvey, A.G., Hill, E.W., and Bayat, A. Designing implant surface topography for improved biocompatibility. Expert Rev Med Devices **10,** 257, 2013.
28. Zhang, W., Ou, J., Inagaki, Y., Greenwel, P., and Ramirez, F. Synergistic cooperation between Sp1 and Smad3/Smad4 mediates transforming growth factor beta1 stimulation of alpha 2(I)-collagen (COL1A2) transcription. J Biol Chem **275,** 39237, 2000.
29. Sysa, P., Potter, J.J., Liu, X., and Mezey, E. Transforming growth factor- b 1 up-regulation by Sp1 and Smad2 transacting factors. DNA Cell Biol **28,** 425, 2009.
30. Verrecchia, F., Chu, M.L., and Mauviel, A. Identification of novel TGF-beta/Smad gene targets in dermal fibroblasts using a combined cDNA microarray/promoter transactivation approach. J Biol Chem **276,** 17058, 2001.
31. Hu, B., Wu, Z., and Phan, S.H. Smad3 mediates transforming growth factor-beta-induced alpha-smooth muscle actin expression. Am J Respir Cell Mol Biol **29,** 397, 2003.
32. Gu, L., *et al.* Effect of TGF-beta/Smad signaling pathway on lung myofibroblast differentiation. Acta Pharmacol Sin **28,** 382, 2007.
33. Ghosh, A.K., Yuan, W., Mori, Y., and Varga, J. Smad-dependent stimulation of type I collagen gene expression in human skin fibroblasts by TGF-beta involves functional cooperation with p300/CBP transcriptional coactivators. Oncogene **19,** 3546, 2000.
34. Margadant, C., and Sonnenberg, A. Integrin-TGF-beta crosstalk in fibrosis, cancer and wound healing. EMBO Rep **11,** 97, 2010.
35. Reynolds, L.E., *et al.* Accelerated re-epithelialization in beta3-integrin-deficient- mice is associated with enhanced TGF-beta1 signaling. Nat Med **11,** 167, 2005.
36. Asano, Y., Ihn, H., Yamane, K., Jinnin, M., and Tamaki, K. Increased expression of integrin αvβ5 induces the myofibroblastic differentiation of dermal fibroblasts. Am J Pathol **168,** 499, 2006.
37. Assoian, R.K., and Klein, E.A. Growth control by intracellular tension and extracellular stiffness. Trends Cell Biol **18,** 347, 2008.
38. Lee, J., Majidi, C., Schubert, B., and Fearing, R.S. Sliding-induced adhesion of stiff polymer microfibre arrays. II. Microscale behaviour. J R Soc Interface **5,** 845, 2008.
39. Livak, K.J., and Schmittgen, T.D. Analysis of relative gene expression data using real-time quantitative PCR and the 2(-Delta Delta C(T)) Method. Methods **25,** 402, 2001.

Address correspondence to:
Tejal Desai, PhD
UCSF Department of Bioengineering
and Therapeutic Sciences
UCSF QB3 Box 2520
1700 4th Street, Rm 204
San Francisco, CA 94158-2330

E-mail: tejal.desai@ucsf.edu

Received: February 23, 2015
Accepted: October 13, 2015
Online Publication Date: December 11, 2015